Improving Integrated Vapour Transport Forecasts over the Himalayas Using a Convolutional Neural Network for Better Atmospheric River Prediction

Sheikh Imran Fayaz[1], Munir Ahmad Nayak[2], Adnan Kaisar Khan[1]

[1]sheikhimranfayaz@gmail.com, [2]munir.nayak@nitsri.ac.in, [1]adnankaisarkhan@gmail.com

This manuscript is a non-peer-reviewed preprint submitted to EarthArXiv.

Keywords

Atmospheric Rivers; Integrated Vapor Transport; Convolutional Neural Network; Numerical Weather Prediction; Himalayas; GFS; Deep Learning

[1]Department of Civil Engineering, National Institute of Technology Srinagar, India, [2] Assistant Professor, Department of Civil Engineering, National Institute of Technology Srinagar, India

Abstract

Extreme precipitation over the Himalayas is often linked to Atmospheric Rivers (ARs) interacting with its unique and complex topography. The topographic complexity and sparse observational data pose a challenge for numerical weather prediction models. We find that the widely used Global Forecast System (GFS) exhibits systematic errors in high-magnitude Integrated Vapor Transport (IVT), and its predicted AR structure and direction show significant mismatches with observations. Our work proposes a modified convolutional neural network model, based on a previously developed ARcnn, for IVT over South Asia, including the Himalayas. ARcnn significantly improves the error metrics, root mean square error (RMSE), bias in high-IVT, and directional mean angular error (MAE), for both 24-hour lead and 7-day lead forecasts over the Himalayan region. The results in this study indicate improved IVT forecasts across the entire study area and more specifically over the Himalayas. Further, the ARcnn model was able to correct IVT that made it possible to detect the ARs missed in GFS forecasts for both lead times. Thus, these results provide compelling evidence of ARcnn's powerful postprocessing capability and its potential for use in early prediction tools for IVT and AR.

1. Introduction

Coherent lower tropospheric structures of large moisture flux flows with length exceeding 2000 km and maximum width of 1000 km are known as Atmospheric Rivers (ARs). These form a major contributor to poleward moisture transport across the midlatitude and synoptic scale moisture circulation (Zhu & Newell, 1998; Guan & Waliser, 2019). ARs have a strong influence over the precipitation trends and alleviating the droughts, but also pose a danger to flooding and landslides (Payne et al., 2020). Over the western coast of the United States, the mean annual precipitation by ARs is about 30–65%. Also, in the west coast of North America, more than 60% of extreme hydrometeorological events are linked to ARs (Lamjiri et al., 2017; Gershunov et al., 2017). In spite of the low occurrence of ARs, these contribute about one-third of annual snow accumulation (Guan et al., 2010). Asia-Pacific region, ARs cause rainfall of about 50–60 mm day^{-1} with their intensities reaching nearly 80 mm day^{-1} when interacting with terrain, and achieve the maximum value when coexisting with tropical cyclones (Wu et al., 2026). These findings highlight the importance of ARs for water management. The strength and associated impacts of ARs are strongly linked with Integrated Vapor Transport (IVT), a metric for AR identification and quantification. Thus, the reliable representation of IVT is fundamental for predicting extreme precipitation, flooding risk, and related hydrological hazards (Ralph et al., 2018).

ARs display a distinct effect over the Himalayan Mountains, where the extreme topography and highly sensitive climate augment the hydrological impacts. The relatively low occurrence of ARs in the Himalayas compared to coastal regions does not reduce their impacts due to the region's steep terrain. This intense effect is characterized by a significant increase in moisture transport and rising freezing levels that drive a critical transition from snow to rain, which reduces frozen precipitation and destabilizes the snowpack (Nayak et al. 2021). The elevated freezing levels increase liquid runoff and rainfall on snow, that increase the glacier melt and alters the mass balance of major river basins like the Brahmaputra, Indus, and Ganges. The Orographic lifting of ARs frequently triggers localized heavy rainfall strongly associated with extreme landfall flooding in India (Mahto et al. 2023). The variations caused to the hydrological cycle by ARs escalate the risk of flash floods and landslides, posing a threat to safety and water security for the vulnerable downstream communities.

The widely used Numerical Weather Prediction (NWP) model is the Global Forecast System (GFS). It is used to predict IVT, but the issue is that it exhibits systematic errors in IVT magnitude and spatial structure. The challenge faced by the GFS is that it struggles to forecast high-magnitude IVT accurately during strong moisture transport events (Chapman et al., 2019). GFS IVT predictions also show frequent spatial displacement of IVT plumes, which is responsible for errors in AR landfall location that reduce the forecast skill for heavy precipitation and flooding (Wick et al., 2013). Beyond the IVT magnitude and position, the orientation of AR, i.e., IVT direction, also plays a significant role in precipitation and determines the rainfall patterns related to the AR. Research shows that two different catchments, Teifi and Dyfi in the UK, produce high precipitation for different AR orientations. This is because if the orientation of the AR is more orthogonal to the terrain, it will cause high precipitation, whereas if it has a more oblique orientation, precipitation response will be weak (Hecht et al. 2017; Griffith et al. 2020). But the zonal (U) and meridional (V) wind components of GFS forecasts (Guo et al., 2024) used directly in IVT calculations also show errors that will be propagated in the moisture transport estimates and will finally affect the AR orientation and associated rainfall. On a broader perspective, the GFS provides reliable IVT predictions, but it continues to exhibit significant errors in IVT magnitude, position, and wind-related components of moisture transport, especially during AR events.

A Convolutional Neural Network (CNN) is a deep learning (DL) framework that recognizes hierarchical features in a gridded image to perform classification or regression tasks. Core components of a CNN consist mainly of three stages, as briefly stated. Convolutional layers, which use kernels, 2D learned weight matrices, to extract features from gridded image data. Pooling layers summarize the features generated to provide distortion invariance. Lastly, the fully connected layers map the final features generated to a final output for a classification task like in healthcare and autonomous systems. This is the structure of early CNNs used for classification, but as research on computer vision progressed, CNNs have been used for regression tasks as well. The "Half-CNN" framework demonstrated that by removing fully connected layers, an image regression CNN model is achieved (Yuan et al. 2014). This framework makes CNNs ideal for spatial prediction regression tasks. Thus, this work adopts a CNN deep learning model for GFS IVT fields post-processing to improve IVT maps for better AR prediction over the Himalayan region.

DL algorithms have emerged as a reliable approach for short-term weather forecasting and AR forecast improvement (Bi, K et al.; Chen, L. et al.; Tian, Y. et al.; Singh, S. et al.). Recently, machine learning weather prediction (MLWP) models, including GraphCast, Pangu-Weather, FuXi, and NeuralGCM, have demonstrated the potential of ML for weather forecasting and AR prediction (Zhang et al., 2025; Swenson et al., 2026). Although these forecasting models have achieved competitive skill, systematic biases in IVT, AR intensity, spatial extent, and landfall location remain, highlighting the need for further regional refinement. Another approach focuses on ML-based post-processing of numerical weather prediction (NWP) forecasts. Most notably, Chapman et al. (2019) introduced a CNN model for post-processing GFS IVT forecasts and demonstrated substantial improvements in IVT magnitude and moisture-transport pathways.

However, this effort was focused on the western United States and eastern Pacific regions. To date, no ML-based AR post-processing model has been adapted and trained for the Himalayas. This highlights the need for a region-specific ML framework for AR post-processing over the Himalayas.

Accordingly, the objective of this research is to adapt the previously developed framework, specifically trained for the region, which includes the Himalayan domain. While existing deep learning models for post-processing IVT and AR data have demonstrated high performance in Western mid-latitude regions, their applicability to the high-altitude complex terrain of South Asia remains limited. As the predefined models are trained on specific regions and also do not correct the direction component, this creates a modeling gap for our region of interest, which is distinct in orographic uplift and AR characteristics, which thus needs to be filled for the Himalayas and the adjoining region. Our modified CNN model fills this gap according to the region's inherent complexities and also corrects the direction of IVT so that a robust region-specific CNN architecture is achieved to process the GFS IVT for accurate IVT and AR prediction.

2. Data

This work utilizes two primary datasets: the Modern-Era Retrospective Analysis for Research and Applications, Version 2 (MERRA-2) and GFS. For the purposes of model training, validation, and testing, the MERRA-2 reanalysis serves as the observational proxy for the ground truth, while GFS IVT forecast fields constitute the input required to be corrected. The time range of data is from 17 January 2015 to 30 April 2025, for the extended cool season (October to April), encompassing the winter peak in AR occurrence over the Himalayas, where AR activity is most prominent during winter (Nayak et al., 2021). Variables required for computing IVT (specific humidity and wind components) were extracted for pressure levels of 1000 hpa to 300 hpa (McCarty et al., 2016; Gelaro et al., 2017). The spatial grid for which data is used extends from 0°N to 40°N latitude and 50°E to 100°E longitude, providing a sufficient buffer region for ARs interacting with the Himalayan region.

2.1 GFS Forecast Data

GFS is an NWP model developed by the National Oceanic and Atmospheric Administration (NOAA) branch of the National Centers for Environmental Prediction (NCEP). GFS operates daily 4 times at 0000, 0600, 1200, and 1800 UTC and provides up to a 16-day forecast (Environmental Modeling Center [EMC], 2016). It forecasts a wide range of atmospheric variables at various spatial and temporal resolutions. The GFS IVT data are extracted from the NCEP GFS Global Forecast Grids Historical Archive at a spatial resolution of 0.25° × 0.25° (UCAR Research Data Archive [RDA], 2024). GFS forecasts are available at 3-hour intervals for lead times up to 240 hours (10 days) and 12-hour intervals from 240 to 384 hours (10–16 days), thus providing both short-term and long-term forecasts. This work initialized the GFS forecast at 0000 UTC with 24-hour and 7-day lead times.

2.2 MERRA-2 Data

The NASA Global Modeling and Assimilation Office (GMAO) developed a modern, high-quality atmospheric reanalysis product known as Modern-Era Retrospective Analysis for Research and Applications, Version 2 (MERRA-2). It incorporates a diverse collection of satellite and ground-based data points using the GEOS-5 data assimilation system, providing temporally consistent fields of atmospheric, land, and oceanic variables from 1980 onwards (Gelaro et al., 2017). The MERRA-2 dataset used in this study, with a spatial resolution of 0.625° × 0.5°, was downloaded from NASA's Goddard Earth Sciences Data and Information Services Center (GES DISC) and utilised for the computation of IVT. To ensure spatial alignment between the MERRA-2 and GFS datasets, the GFS data (spatial resolution: 0.25° × 0.25°) were regridded to the MERRA-2 grid resolution using the second-order conservative remapping method. This method conserves integral quantities such as fluxes and minimises spatial interpolation errors, which permits a reliable comparison between forecasted and reanalysis-derived IVT fields.

3. Method

IVT consists of two components: magnitude and direction. The former represents the strength of IVT plumes, and the latter represents the orientation of moisture fluxes. To correct the biases in both components, we develop two CNN models, collectively referred to as the ARcnn model. The first model, named the ARcnn magnitude model, corrects the magnitude of IVT fields, while the second model, referred to as the ARcnn direction model, corrects the IVT direction vectors. The outputs from both models were combined, the magnitude field and the direction field, to obtain bias-corrected IVT fields with improved prediction of intensity and direction of IVT plumes. The architecture of the ARcnn model is depicted in Figure 1 and Figure 2; for a detailed discussion of the model, refer to supplementary Text S1 and S2.

For developing the ARcnn model framework, the dataset was divided into training, validation, and testing subsets chronologically, following an 85:5:10 split, respectively. The training, validation, and testing datasets range from 17 January 2015 to 29 December 2023, 30 December 2023 to 17 April 2024, and 18 April 2024 to 30 April 2025, respectively. The ARcnn model is trained separately for 24-hour and 7-day lead times. For each lead time, the GFS and MERRA-2 IVT fields are paired such that each GFS forecast with a lead time corresponds to the same-date MERRA-2 IVT field, forming valid input–target pairs for model training. After the model training for two different lead times, we will obtain two different sets of weights: one for 24-hour lead forecasts and the other for 7-day lead forecasts.

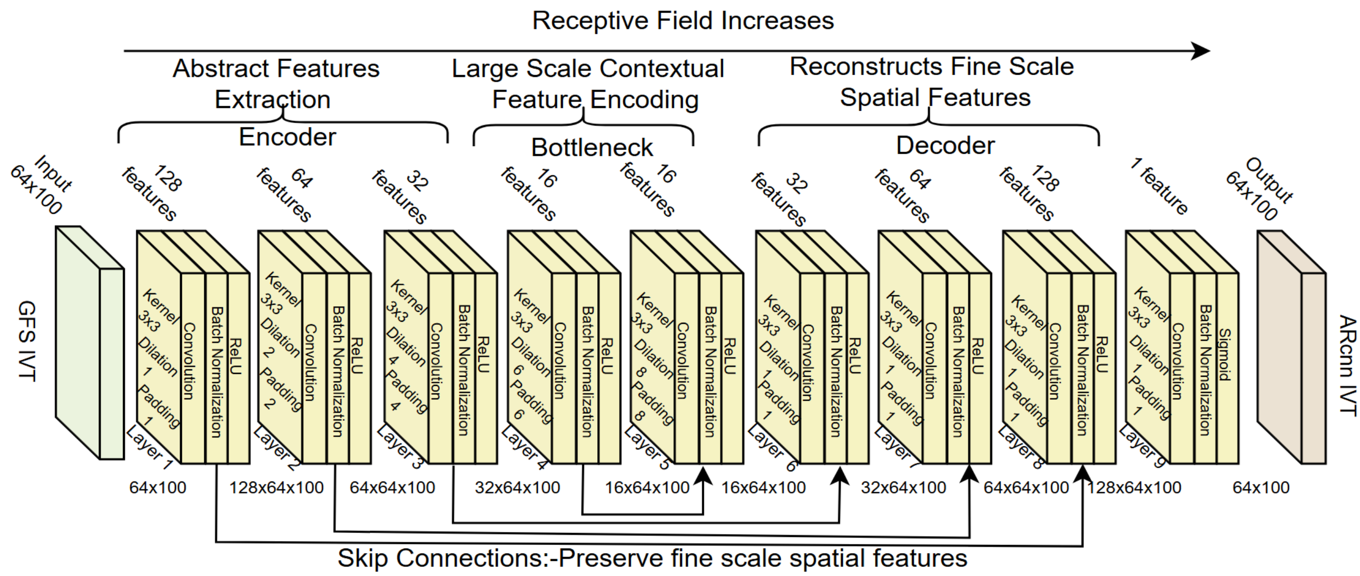

Figure 1. Architecture of ARcnn architecture showing details of features, dilation, padding, kernel in each layer and skip

connections

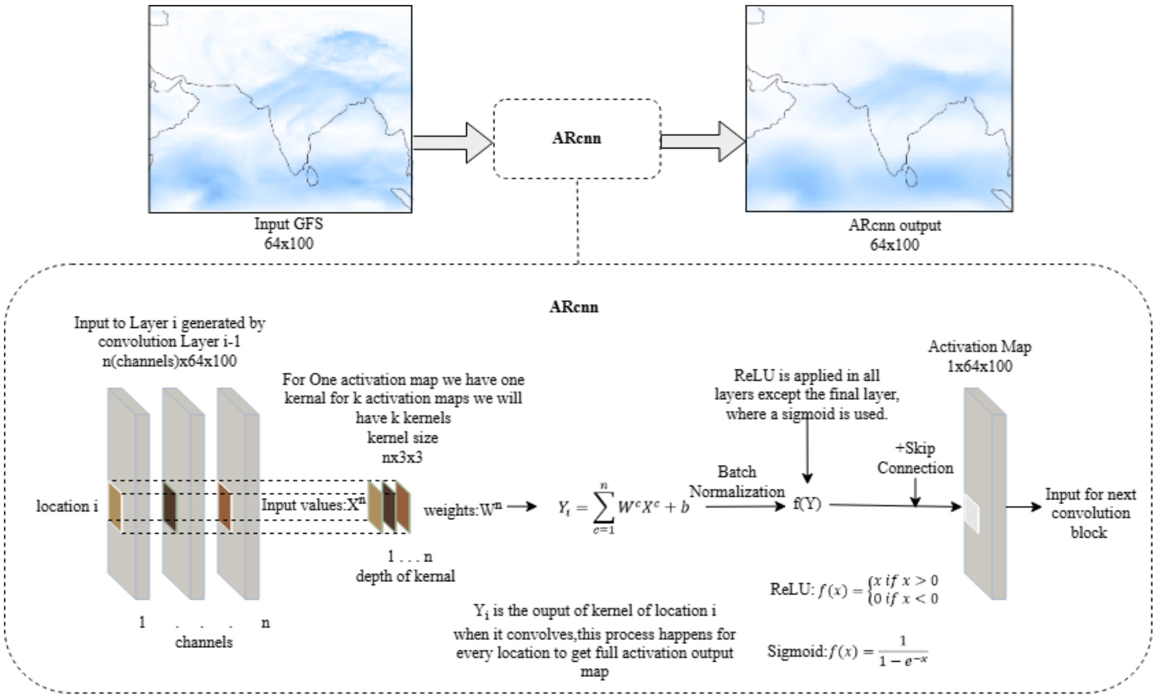

Figure 2. layer-wise operations of the ARcnn model for a single convolutional kernel, resulting in one activation (output feature) map. This same process is repeated independently for each kernel in the layer, such that the total number of activation maps produced equals the number of output channels of that layer.

3.1 Metrics Used for Model Evaluation

For the test period, 24-h and 7-day lead GFS IVT forecasts were evaluated against the corresponding MERRA-2 IVT fields, which serve as the reference dataset. The performance of the ARcnn IVT magnitude model and GFS model IVT forecasts was quantified using four widely adopted statistical metrics: Root Mean Square Error (RMSE), Centered Root Mean Square Error (CRMSE), Bias, and Pearson Correlation (PC). Afterwards, the metrics were eventually used to quantify the percentage improvement achieved by the ARcnn postprocessing with respect to the baseline GFS forecasts.

The performance of the ARcnn IVT direction model and GFS IVT direction fields was assessed using the Mean Angular Error (MAE), which measures the average angular difference between the predicted (ARcnn or GFS IVT directions) and reference IVT direction vectors (MERRA-2 IVT directions). This metric directly evaluates the accuracy of directional correction independent of IVT magnitude and provides a physically meaningful assessment of improvements in moisture transport orientation.

4. Results

The evaluation of the model performance is conducted in a staged approach, beginning with each metric assessment before moving to the validation of atmospheric river (AR) events. In the first stage, the ARcnn magnitude and ARcnn direction models are evaluated as independent CNN models using the statistical metrics previously defined. After the individual performance of these models is established, the combined ARcnn output (magnitude model + direction model) is applied to specific AR events. To detect ARs in the dataset, we leverage the AR detection method developed by Guan and Waliser (2019) and implemented by Kennett (2021). Using this algorithm, first the ARs are detected in the reanalysis test dataset, which serves as a reference. Then the corresponding GFS and ARcnn-corrected IVT fields are evaluated on the same dates to compare their ability to reproduce the reference ARs and to quantify the improvements achieved by ARcnn over GFS in IVT representation within the detected AR boundaries. This targeted analysis assesses whether ARcnn effectively captures the intense moisture transport gradients and directional coherence necessary for accurate Himalayan AR forecasting.

4.1 ARcnn Magnitude Model Validation

For the evaluation of post-processed ARcnn IVT and GFS IVT forecast predictive skills, spatial error maps were plotted for the test set on the domain of analysis. Standard evaluation metrics: Root Mean Square Error (RMSE), Centered Root Mean Square Error (CRMSE), Bias, and Pearson Correlation (PC) were calculated in the form of spatial maps. These maps were utilized to visualize and compare the metrics between the GFS and ARcnn models.

For 24-hour lead forecasts, Figure 3 shows spatial maps of the RMSE and Bias evaluation of GFS IVT and ARcnn postprocessed IVT with respect to MERRA-2, along with the corresponding improvement maps of the ARcnn IVT field with respect to GFS IVT. Bias assessment is restricted to IVT magnitudes ≥ 100 kg m^{-1} s^{-1}. This thresholding ensures the evaluation remains focused on the high-IVT regimes that are fundamental to ARs. By screening out low-intensity IVT background noise that displays nominal bias shifts or minor degradation, the training prioritizes the core IVT cluster that drives AR body rather than the peripheral zones where minor IVT errors are trivial. Similarly, Figure S1 shows spatial maps of PC and CRMSE for GFS, ARcnn, and the corresponding improvement maps. Lower values in Figure 3(c) and (d) compared to Figure 3(a) and (b) indicate that ARcnn improves the representation of IVT across both the entire domain and the Himalayan region. This improvement is shown by the blue colours in Figure 3(e) and (f). Similarly, improvements in PC and CRMSE are observed in Figure S1.

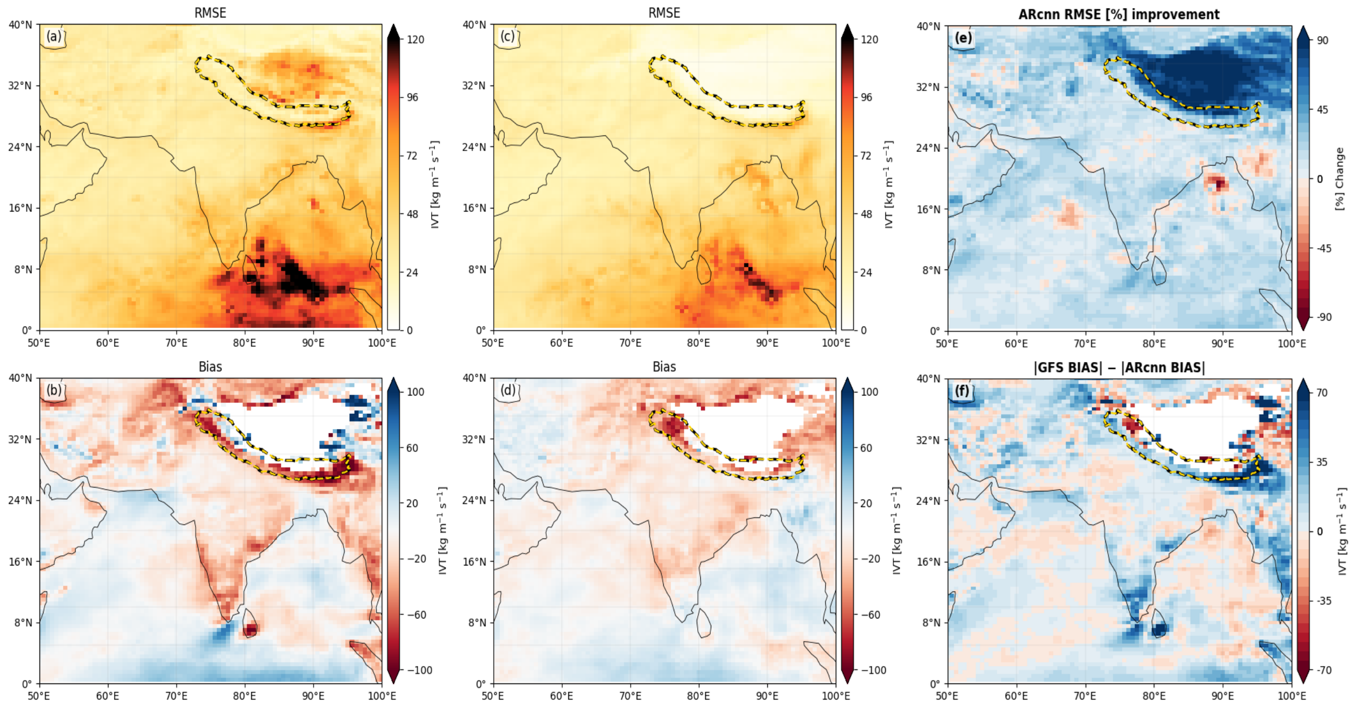

Figure 3. For 24-hour lead forecasts, spatial distribution of RMSE and Bias for GFS and ARcnn. Panels (a) and (c) show RMSE of GFS and ARcnn, respectively, and panels (b) and (d) show Bias of GFS and ARcnn, respectively. In the Bias panels, positive values (blue) indicate overestimation and negative values (red) indicate underestimation. The yellow-black dashed boundary represents the Himalayan region. Panels (e) and (f) indicate improvement of ARcnn IVT in RMSE and Bias with respect to GFS IVT, as shown by blue colours.

For 7-day lead forecasts, Figure 4 presents similar spatial maps to Figure 3, while Figure S2 shows spatial maps of PC and CRMSE metrics. The dominant blue colours in Figure 4(e) and (f), as well as in Figure S2(e) and (f) across the entire domain and the Himalayas, indicate that ARcnn improves the IVT field relative to GFS IVT.

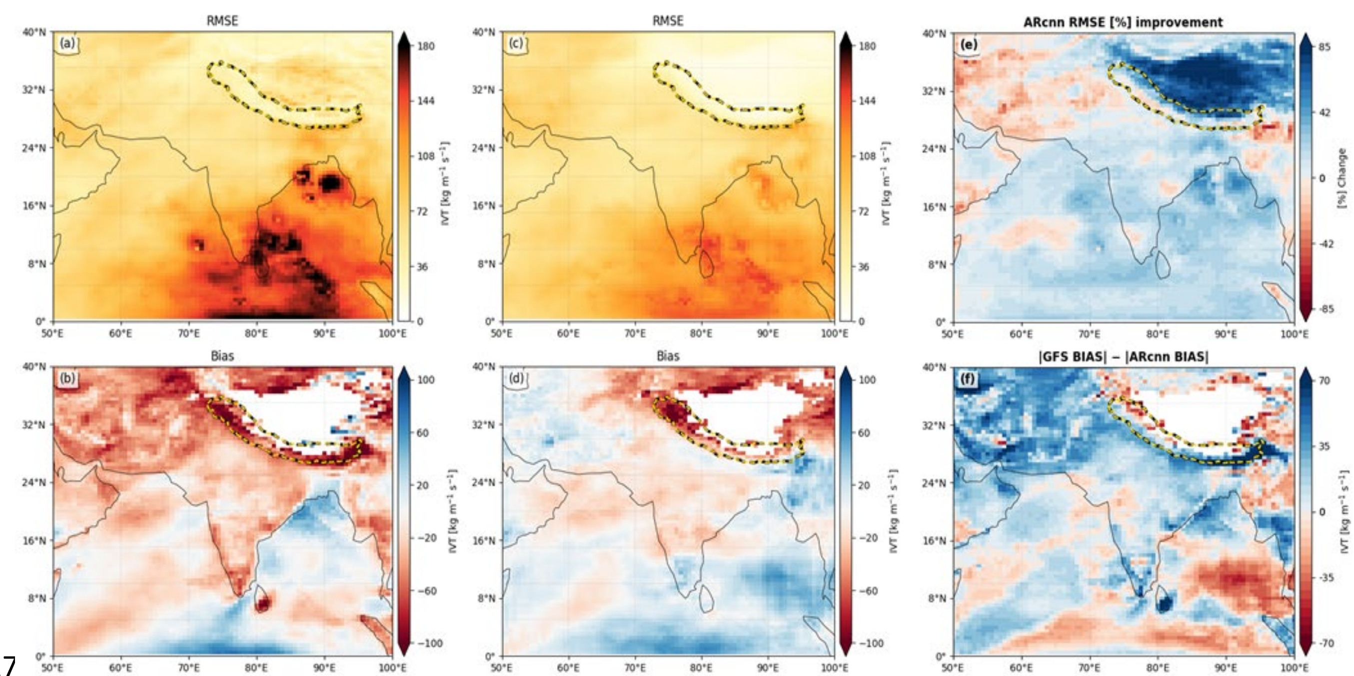

Figure 4. Same as Figure 3, but for the 7-day lead forecasts.

To quantify the mean improvement in evaluation metrics across the entire domain and the Himalayan region, spatially averaged values for each metric were computed from corresponding spatial distribution maps for both regions. The results are summarized in Table 1.

Table 1. Domain-averaged IVT magnitude metrics for the GFS and ARcnn magnitude model and the corresponding percentage improvement of the ARcnn magnitude model relative to the GFS.

Lead Time	Region	Metric	GFS	ARcnn	Improvement (%) (ARcnn vs GFS)
7-day	Himalayan Region	RMSE (kg m^{-1} s^{-1})	41.8	32.7	**21.7**
		CRMSE (kg m^{-1} s^{-1})	36.3	29.9	**17.4**
		Bias (IVT ≥ 100)	−72.5	−48.5	**33.1**
		Pearson Correlation (PC)	0.40	0.49	**21.6**
	Full Domain	RMSE (kg m^{-1} s^{-1})	83.5	71.3	**14.7**
		CRMSE (kg m^{-1} s^{-1})	81.2	65.8	**18.8**
		Bias (IVT ≥ 100)	−36.4	−11.7	**67.7**
		Pearson Correlation (PC)	0.58	0.65	**10.2**
24-hour	Himalayan Region	RMSE (kg m^{-1} s^{-1})	34.6	20.2	**41.6**
		CRMSE (kg m^{-1} s^{-1})	28.2	19.7	**30.0**
		Bias (IVT ≥ 100)	−46.5	−34.1	**26.9**
		Pearson Correlation (PC)	0.643	0.786	**22.2**
	Full Domain	RMSE (kg m^{-1} s^{-1})	47.6	37.8	**20.6**
		CRMSE (kg m^{-1} s^{-1})	44.7	37.1	**17.3**
		Bias (IVT ≥ 100)	−17.6	−11.8	**32.7**
		Pearson Correlation (PC)	0.85	0.89	**4.9**

4.2 ARcnn Direction Model Validation

Since the orientation of AR is a significant component for precipitation associated with it, the IVT direction improvement is also necessary for better predictability of ARs as well as precipitation (Hecht, C. W. et al.; Griffith HV et al).To evaluate the performance of the ARcnn direction model, the mean angular error (MAE) of the IVT direction is computed at each grid point for both the GFS forecasts and the ARcnn-corrected fields, with respect to MERRA-2, using the independent test dataset. The resulting spatial maps provide a clear comparison of directional errors across the entire study domain as well as the Himalayan region.

Figure 5 is evident in drawing the conclusion that the ARcnn direction model achieves a clear reduction in MAE across both the entire domain and the Himalayan region. The improvement is visually apparent from the lower values in Figure 5(b) compared to Figure 5(a), indicating lower directional errors relative to the GFS baseline.

Figure 5(c) in both the top and bottom rows highlights the widespread improvement, with blue shading prominent in both the Himalayan region and large portions of the full domain, indicating substantial percentage reductions in MAE achieved by the ARcnn model. These results establish the enhanced capability of the ARcnn direction model to correct IVT directional errors, particularly over the complex terrain of the Himalayas.

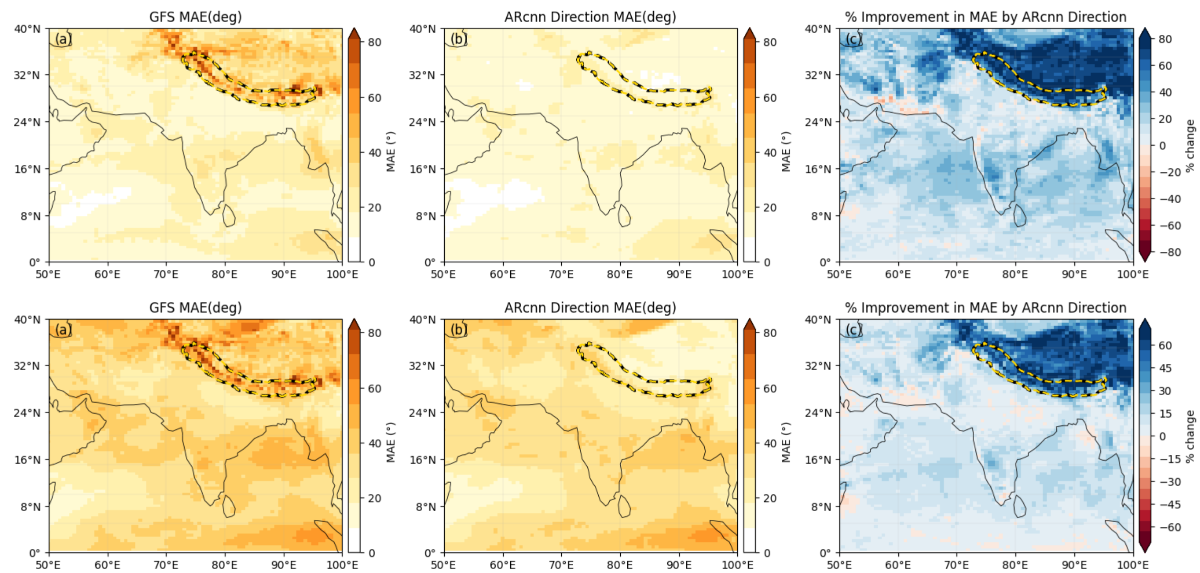

Figure 5. Spatial distribution of mean angular error (MAE) in IVT direction for 24-hour (top row) and 7-day (bottom row) lead forecasts. Panels (a) and (b) show MAE for the GFS forecast and the ARcnn direction model, respectively, both evaluated against MERRA-2. In panels (a) and (b), lighter colors indicate smaller directional errors, while darker colors denote larger errors. Panel (c) shows the percentage change in MAE achieved by the ARcnn direction model relative to GFS, where blue colors indicate improvement (error reduction) and red colors indicate degradation. The yellow–black dashed outline marks the Himalayan region.

Table 2 summarizes the entire region-averaged MAE of IVT direction for the GFS forecast and the ARcnn direction model over both the entire region and the Himalayan region for 24-hour and 7-day lead forecasts. The results show that ARcnn consistently outperforms GFS across both lead times. For the 24-hour lead, the mean directional error is reduced by 24.4% over the full domain and by 59.2% over the Himalayan region. Likewise, for the 7-day lead forecast, ARcnn reduces the directional error by 15.1% over the full domain and by 44.8% over the Himalayan region. These enhancements establish the improved capability of the ARcnn direction model to correct IVT flow direction, particularly over complex topography such as the Himalayas.

Table 2. Region-averaged IVT direction MAE for GFS and ARcnn Direction model, and the corresponding improvement of ARcnn Direction model over GFS for the full domain and the Himalayan region.

Lead Time	Region	GFS MAE (°)	ARcnn MAE (°)	Absolute Improvement (°)	Percentage Improvement (%)
24-hour	**Himalayan**	45.1	16.5	28.5	**59.2**
	Entire	22.2	15.1	7.1	**24.4**
7-day	**Himalayan**	51.8	27.2	24.6	**44.8**
	Entire	36.7	30.4	6.3	**15.1**

4.3 ARcnn Model Performance for AR Events

Landfalling Atmospheric River (AR) events in the test dataset are identified using the algorithms by Guan and Waliser (2019) and Kennett (2021). A total of three landfalling AR events are identified during the test period. These events are used as a case study to evaluate whether the improvements in IVT by ARcnn are translated into improved AR detection. For these events, RMSE, CRMSE, bias, and Pearson correlation are computed within the AR region for both the GFS forecasts and the ARcnn post-processed IVT fields with respect to MERRA-2. In addition, ARs detected in ARcnn IVT fields are visually compared with corresponding GFS and MERRA-2 fields to qualitatively examine improvements in AR structure and intensity.

GFS forecasts, respectively. In both cases, the AR is detected in the ARcnn postprocessed IVT field, which couldn't be detected in the GFS IVT field. In Figure 6, for the 24-hour lead forecast, the mean GFS IVT forecast is underestimated by 11.6% in the AR field, whereas in the ARcnn postprocessed IVT field there is reduced underestimation of 7.0%; this improvement with respect to the GFS IVT corresponds to 5.3%. Similarly, for the 7-day GFS lead forecast in Figure 7, the underestimation by GFS becomes more pronounced, with a mean IVT underestimation of 25.6%. The ARcnn IVT field has an underestimation of 20% and delivers an improvement of 7.4% relative to the GFS forecast.

Across all three landfalling AR events identified in the test set, the ARcnn model demonstrates substantial and consistent improvements over the baseline GFS forecasts within the AR regions, as summarized in Table 3 and Table 4. For the 24-hour lead forecasts, in the GFS IVT fields only one of the three observed AR events is detected (Figure S3(b)), whereas in the ARcnn-corrected IVT fields all three AR events were detected (Figure 6(c), S3(c), and S4(c)). For the 7-day lead forecasts, in the baseline GFS IVT none of the three ARs were detected, whereas one AR event is successfully detected in the corrected ARcnn IVT field (Figure 7(c)). These results indicate that the improved IVT magnitude and direction produced by ARcnn enhance the representation of AR structures, particularly at shorter lead times.

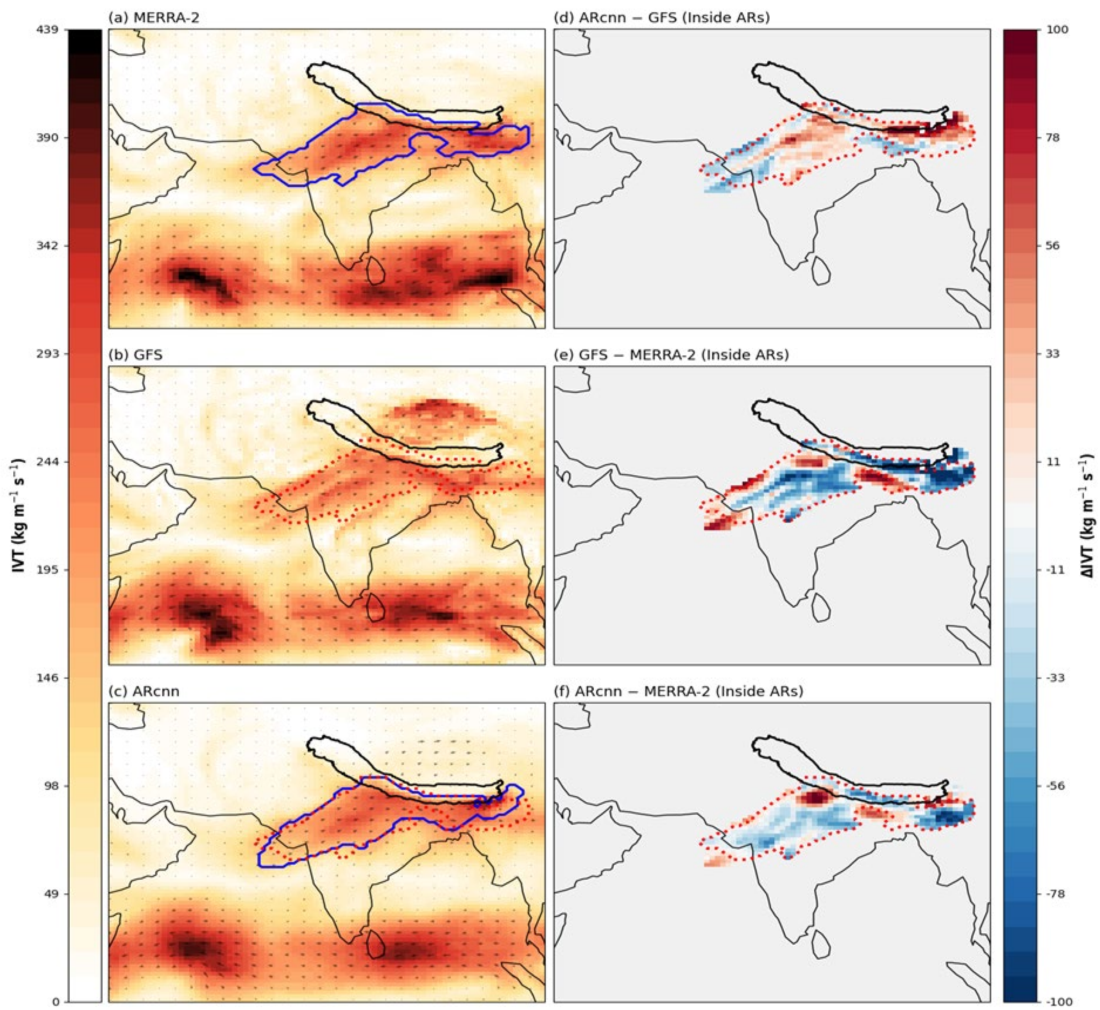

Figure 6. Atmospheric River (AR) event on 16 March 2025 identified using different models for 24-hour lead time. Panel (a) shows the MERRA-2 IVT field, blue boundary represents AR detected in MERRA-2, which serves as the reference AR. Panel (b) shows the GFS IVT forecast, AR was not detected, and the red dotted boundary represents the reference AR. Panel (c) shows that the ARcnn IVT field, where AR is successfully detected, shown in the blue boundary. Panel (d) displays the IVT difference between ARcnn and GFS (ARcnn − GFS) within the AR region, highlighting the amount of correction introduced by ARcnn. Panels (e) and (f) show GFS − MERRA-2 and ARcnn − MERRA-2 IVT differences, respectively. The lighter colors in (f) compared to (e) indicate reduced IVT errors, confirming that ARcnn improves both IVT magnitude and direction, enabling successful detection of an AR event missed by GFS. The red dashed line denotes the MERRA-2-detected AR overlaid on all panels, and the black boundary outlines the Himalayan region.

Table3: Metrics for IVT in AR regions in test set for 24-hour lead GFS

Metric	GFS	ARcnn	Change (ARcnn − GFS)
Mean Bias(kg m⁻¹ s⁻¹)	−13	−11.3	**+1.7(13.2%)**
RMSE (kg m⁻¹ s⁻¹)	57.5	42.9	**25.3%**
CRMSE (kg m⁻¹ s⁻¹)	54.8	40.8	**25.6%**
Pearson Correlation	0.69	0.83	**+0.14(20%)**

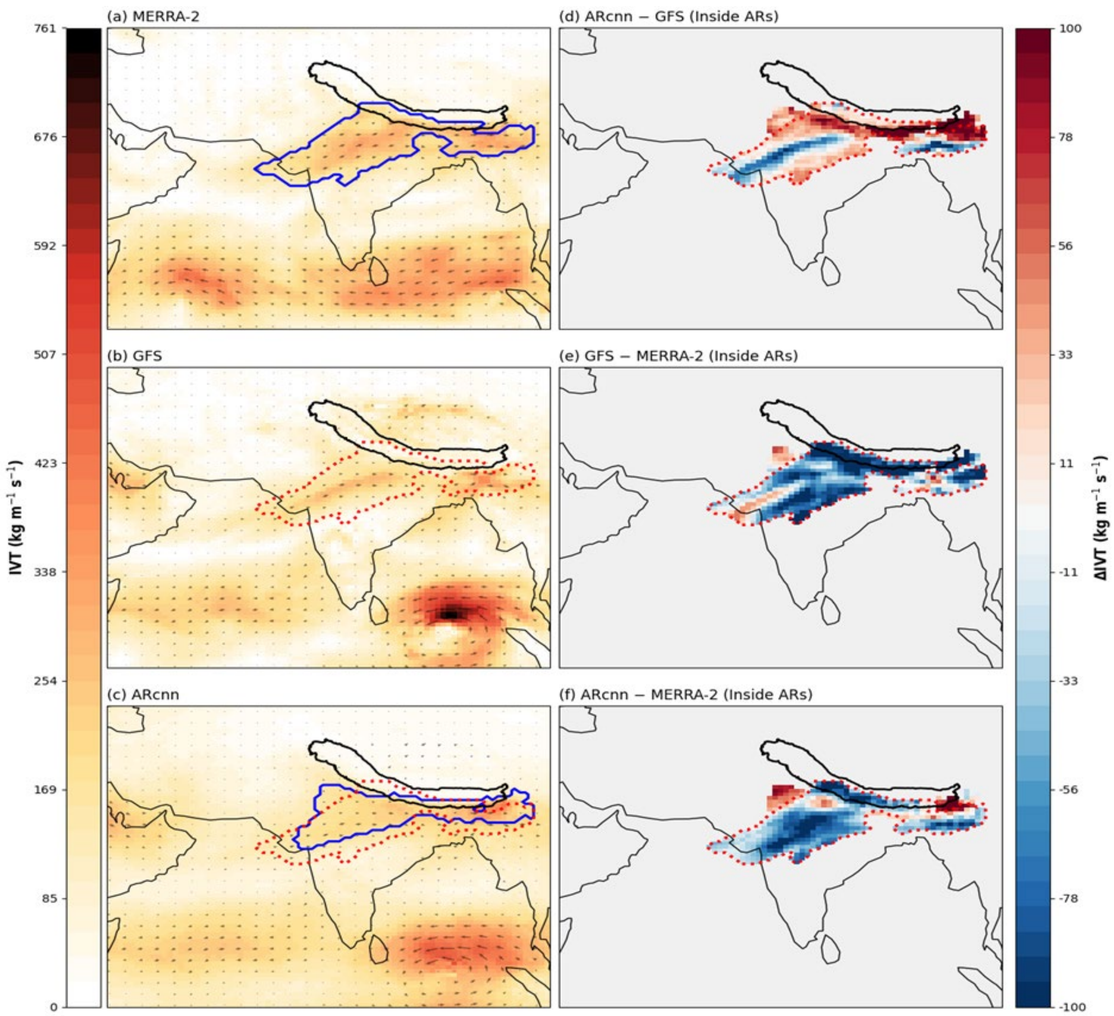

Figure 7. same as Figure 6 for 7-day lead time GFS forecast.

Table 4: Metrics for IVT in AR regions in test set for 7-day lead GFS

Metric	GFS	ARcnn	Change (ARcnn − GFS)
Mean Bias (kg m^{-1} s^{-1})	−21.5	−17.1	**+4.4 (20.5%)**
RMSE (kg m^{-1} s^{-1})	87.1	65.8	**24.4%**
CRMSE (kg m^{-1} s^{-1})	73.8	50.5	**31.5%**
Pearson Correlation	0.62	0.75	**+0.131 (21.2%)**

The results presented in this section show that GFS IVT forecasts exhibit larger errors in the AR regions and generally underpredict IVT values in these regions. In contrast, ARcnn reduces these errors, resulting in a more accurate representation of moisture transport associated with ARs. As a result, all three ARs are identified in 24-hour lead forecasts, compared with only one event identified in the corresponding GFS IVT fields. For the 7-day lead forecasts, although the improvement was modest, one AR was detected in ARcnn IVT fields, whereas no ARs were detected in the GFS fields. Overall, these observations indicate that improved ARcnn IVT enhances the representation of AR intensity and spatial structure, with a more pronounced effect for 24-hour lead AR events.

5. Discussion

Compared with the improvements in IVT forecast by Chapman et al 2019., who reported an improvement of 9–17% in RMSE and 0.5–12% in PC across 3-hour to 7-day lead times, our model achieves 15-20% and 22-41% improvements in RMSE over the entire domain and the Himalayan region, respectively, and improvements in PC of 5-10% and 20% over the entire and the Himalayan regions, respectively, across 24-hour and 7-day leads. These numbers demonstrate consistent or better improvement over the entire domain, and over the Himalayas, performance is further enhanced. Further, the bias metric is the weakest corrected metric in the previous study and stalls after day 5, but our model reduces the bias by about 25-67%.

Importantly, direction correction was not incorporated in the previous study; our model corrects the MAE by about 15-24% for the entire domain and 45-59% for the Himalayan region. This is extremely important for AR rainfall determination, especially in mountainous regions like the Himalayas, as the orientation of an AR decides heavy precipitation patterns (Hecht et al. 2017; Griffith et al. 2020). As these results and comparison strongly suggest the improvement of ARcnn in correcting MAE, bias, and other metrics, for this reason, the ARcnn was able to correct the IVT of ARs, which were not detected in GFS for both 24-hour and 7-day lead.

The relatively small number of ARs in the test set, due to the relatively limited availability of high-resolution 0.25° GFS data from 2015 onwards, constrains a comprehensive evaluation of AR detection performance using corrected IVT fields. Nevertheless, the available AR events demonstrate the potential of the model for correcting IVT for AR detection and improvement. This limitation could be addressed by generating long-term hindcast forecasts, thereby increasing the number of AR events available for model development and evaluation. Additionally, training and evaluation of the model using a large dataset consisting of AR events only, generated through hindcasting, may further improve the model's ability to correct IVT fields during atmospheric river conditions.

6. Conclusion

The results presented in the research deliver convincing evidence that the convolutional neural network model (ARcnn) delivers significant and physically coherent improvements over the baseline GFS IVT forecasts. By separately correcting IVT magnitude and direction and integrating these components, ARcnn attains systematic error reduction while conserving the spatial structure essential for AR detection for both short-term (24-hour) and long-term (7-day) leads. Importantly, ARcnn significantly reduces errors in IVT direction present in the GFS forecasts. Accurate representation of IVT direction is particularly important because the orientation of an AR relative to topographic barriers determines the magnitude of precipitation and the associated hydrological impacts.

Event-based analysis of ARs demonstrates the potential of ARcnn to reinforces moisture transport intensity, reduces AR-region RMSE and CRMSE, and significantly improve the spatial coherence of IVT. The improved ARcnn IVT outputs are more suitable for AR identification than the raw GFS forecasts. In general, the ARcnn model is a robust post-processing tool that improves the accuracy and physical realism of IVT forecasts over the Himalayas. The study emphasizes the strong potential of deep learning-based correction algorithms to complement NWP systems for topographically complex and data-sparse regions, with direct consequences for hydrological hazard prediction and early warning systems.

7. References

Bi, K., Xie, L., Zhang, H. et al. Accurate medium-range global weather forecasting with 3D neural networks. Nature 619, 533–538 (2023). https://doi.org/10.1038/s41586-023-06185-3

Chapman, W. E., Delle Monache, L., Alessandrini, S., Subramanian, A. C., Ralph, F. M., Xie, S.-P., Lerch, S., & Hayatbini, N. (2022). Probabilistic predictions from deterministic atmospheric river forecasts with deep learning. Monthly Weather Review, 150(1), 215–234. https://doi.org/10.1175/MWR-D-21-0106.

Chapman, W. E., Subramanian, A. C., Delle Monache, L., Xie, S.-P., & Ralph, F. M. (2019). Improving atmospheric river forecasts with machine learning. Geophysical Research Letters, 46(17–18), 10627–10635. https://doi.org/10.1029/2019GL083662

Chen, L., Zhong, X., Zhang, F. et al. FuXi: a cascade machine learning forecasting system for 15-day global weather forecast. npj Clim Atmos Sci 6, 190 (2023). https://doi.org/10.1038/s41612-023-00512-1

Environmental Modeling Center (EMC). (2016). Global Forecast System (GFS) model description. National Centers for Environmental Prediction (NCEP), NOAA.

Gelaro, R., McCarty, W., Suárez, M. J., et al. (2017). MERRA-2: Modern-Era Retrospective Analysis for Research and Applications, Version 2. Journal of Climate, 30(14), 5419–5454. https://doi.org/10.1175/JCLI-D-16-0758.1

Gershunov, A., Shulgina, T., Ralph, F. M., Lavers, D. A., & Rutz, J. J. (2017). Assessing the climate-scale variability of atmospheric rivers affecting western North America. Geophysical Research Letters, 44, 7900–7908. https://doi.org/10.1002/2017GL074175

Glorot, X., Bordes, A., & Bengio, Y. (2011). Deep sparse rectifier neural networks. https://proceedings.mlr.press/v15/glorot11a/glorot11a.pdf

Griffith HV, Wade AJ, Lavers DA, Watts G. (2020). Atmospheric river orientation determines flood occurrence. Hydrological Processes. 2020;34:4547–4555. https://doi.org/10.1002/hyp.13905

He, K., Zhang, X., Ren, S., & Sun, J. (2015). Deep residual learning for image recognition. In Proceedings of the IEEE Conference on Computer Vision and Pattern Recognition (CVPR) (pp. 770–778). https://doi.org/10.1109/CVPR.2016.90

Hecht, C. W., and J. M. Cordeira (2017), Characterizing the influence of atmospheric river orientation and intensity on precipitation distributions over North Coastal California, Geophys. Res. Lett., 44, 9048–9058, https://doi.org/10.1002/2017GL074179

Khan, A., Sohail, A., Zahoora, U. et al. A survey of the recent architectures of deep convolutional neural networks. Artif Intell Rev 53, 5455–5516 (2020). https://doi.org/10.1007/s10462-020-09825-6

Lamjiri, M. A., Dettinger, M. D., Ralph, F. M., & Guan, B. (2017). Hourly storm characteristics along the U.S. West Coast: Role of atmosphericrivers in extreme precipitation. Geophysical Research Letters, 44, 7020–7028. https://doi.org/10.1002/2017GL074193

Mahto, S. S., Nayak, M. A., Lettenmaier, D. P., & Mishra, V. (2023). Atmospheric rivers that make landfall in India are associated with flooding. Communications Earth & Environment, 4, Article 135. https://doi.org/10.1038/s43247-023-00775-9

Nash, D., Carvalho, L. M. V., Rutz, J. J., & Jones, C. (2023). Influence of the freezing level on atmospheric rivers in High Mountain Asia: WRF case studies of orographic precipitation extremes. Climate Dynamics, 62, 589–607. https://doi.org/10.1007/s00382-023-06929-x

Nayak, M. A., Azam, M. F., & Lyngwa, R. V. (2021). ERA5-based database of Atmospheric Rivers over Himalayas. Earth System Science Data Discussions. https://doi.org/10.5194/essd-2020-397

Payne, A.E., Demory, M.-E., Leung, L.R., Ramos, A.M., Shields, C.A., Rutz, J.J., Siler, N., Villarini, G., Hall, A. and Ralph, F.M., 2020. Responses and impacts of atmospheric rivers to climate change. Nature Reviews Earth & Environment, 1, pp.143–157. https://doi.org/10.1038/s43017-020-0030-5

Ralph, F. M., Rutz, J. J., Cordeira, J. M., Dettinger, M., Anderson, M., Reynolds, D., et al. (2018). A scale to characterize the strength and impacts of atmospheric rivers. https://doi.org/10.1175/BAMS-D-18-0023.1

Guan.B, Noah P. Molotch, et al. (2010). Extreme snowfall events linked to atmospheric rivers and surface air temperature via satellite measurements. **https://doi.org/10.1029/2010GL044696**

ScienceDirect (2024). Sigmoid Function. Available at: https://www.sciencedirect.com/topics/computer-science/sigmoid-function [Accessed 24 Oct. 2023].

Swenson, L. M., Moore, B. J., & Mahoney, K. (2026). Atmospheric Rivers in Machine Learning Weather Models. Weather and Forecasting. Advance online publication. https://doi.org/10.1175/WAF-D-25-0142.1

Ioffe, S., & Szegedy, C. (2015). Batch normalization: Accelerating deep network training by reducing internal covariate shift. In Proceedings of the 32nd International Conference on Machine Learning (ICML) (pp. 448–456). https://doi.org/10.48550/arXiv.1502.03167

Shuchang Guo, Yi Yang, Peng Liu Assimilation of the deep learning-corrected global forecast system fields into the regional model for improving medium-range persistent precipitation forecasts https://doi.org/10.1016/j.atmosres.2024.107318

Yuan, J., Ni, B., & Kassim, A. A. (2014). Half-CNN: A general framework for whole-image regression. National University of Singapore. https://doi.org/10.48550/arXiv.1412.6885

Singh, S. & Goyal, M. K. An innovative approach to predict atmospheric rivers: Exploring convolutional autoencoder. Atmos. Res. 289, 106754 (2023). https://doi.org/10.1016/j.atmosres.2023.106754

Tian, Y., Zhao, Y., Son, S.-W., Luo, J.-J., Oh, S.-G., & Wang, Y. (2023). A deep-learning ensemble method to detect atmospheric rivers and its application to projected changes in precipitation regime. Journal of Geophysical Research: Atmospheres, 128, e2022JD037041. https://doi.org/10.1029/2022JD037041

UCAR Research Data Archive (RDA). (2024). NCEP GFS Global Forecast Grids Historical Archive. University Corporation for Atmospheric Research. https://rda.ucar.edu

Yu, F., & Koltun, V. (2015). Multi-scale context aggregation by dilated convolutions. https://doi.org/10.48550/arXiv.1511.07122

Kennett, D. (2021). AR_Detection: Atmospheric River detection algorithm (Version 1.0.0) [Computer software]. GitHub. https://github.com/daemonkennett/ar_detection

Guan, B., & Waliser, D. E. (2019). Tracking atmospheric rivers globally: Spatial distributions and temporal evolution of life cycle characteristics. Journal of Geophysical Research: Atmospheres, 124(23), 12523–12552. https://doi.org/10.1029/2019JD031205

Wick, G. A., P. J. Neiman, F. M. Ralph, and T. M. Hamill, 2013: Evaluation of forecasts of the water vapor signature of atmospheric rivers in operational numerical weather prediction models. Weather and Forecasting, 28, 1337–1352. https://doi.org/10.1175/WAF-D-13-00025.1

Wu, D.-R., Chen, C.-T., & Huang, W.-R. (2026). Characteristics of atmospheric rivers over the Asia–Pacific monsoon region with the modified AR detection algorithm. Journal of the Meteorological Society of Japan, 104, Article 2. https://doi.org/10.1007/s44394-025-00005-0

Xu, G., Wang, X., Wu, X., Leng, X., & Xu, Y. (2025).Development of skip connection in deep neural networks for computer vision and medical image analysis: A survey. https://doi.org/10.1016/j.engappai.2024.109890

McCarty, W., Coy, L., Gelaro, R., Huang, A., Merkova, D., Smith, E. B., et al. (2016). MERRA-2 input observations: Summary and assessment.Technical Report Series on Global Modeling and Data Assimilation,46(October). Retrieved from). https://gmao.gsfc.nasa.gov/pubs/docs/McCarty885.pdf

Zhu, Y., & Newell, R. E. (1998). A proposed algorithm for moisture fluxes from atmospheric rivers. Geophysical Research Letters. https://doi.org/10.1175/1520-0493(1998)126<0725:APAFMF>2.0.CO;2

Zhang, L., Lu, M., Bao, Q., Zhao, Y., & Yang, J. (2025). Global performance benchmarking of artificial intelligence models in atmospheric river forecasting. Communications Earth & Environment, 6, 894. https://doi.org/10.1038/s43247-025-02823-y